Improved High Efficiency Stacked Microstructured Neutron Detectors Backfilled With Nanoparticle ^{6}LiF

S. L. Bellinger, *Member, IEEE*, R. G. Fronk, W. J. McNeil, T. J. Sobering, and D. S. McGregor, *Member, IEEE*

Abstract—Silicon diodes with large aspect ratio trenched microstructures, backfilled with ^{6}LiF, show a dramatic increase in thermal neutron detection efficiency beyond that of conventional thin-film coated planar devices. Described in this work are advancements in the technology using detector stacking methods to increase thermal neutron detection efficiency, along with the current process to backfill ^{6}LiF into the silicon microstructures. The highest detection efficiency realized thus far is over 42% intrinsic thermal neutron detection efficiency by device-stacking methods. The detectors operate as conformally diffused *pn* junction diodes each having 1 cm^2 area. Two individual devices were mounted back-to-back with counting electronics coupling the detectors together into a single dual-detector device. The solid-state silicon device was operated at 3 V and utilized simple signal amplification and counting electronic components that have been adjusted from previous work for slow charge integration time. The intrinsic detection efficiency for normal-incident 0.0253 eV neutrons was found by calibrating against a ^{3}He proportional counter.

Index Terms—Neutron detector, semiconductor radiation detectors, silicon radiation detectors.

I. INTRODUCTION

MICROSTRUCTURED semiconductor neutron detectors (MSND) have been developed and studied at Kansas State University for many years [1]–[5], with much improvement in recent years [6]–[8]. The microstructured detector design offers a viable solution to the efficiency limitations of coated planar diodes, a limitation no greater than 5%. The microstructured detector concept is understood as a method to improve detection efficiency [10]–[12], with the first such device demonstrated nearly a decade ago [1]. Other groups are also investigating variant MSND device designs [13]–[15].

The devices are constructed by etching microstructured features into a semiconductor substrate, diffusing a *pn* junction within the microstructures, and subsequently backfilling the etched features with neutron reactive material. An individual device has the potential of achieving intrinsic thermal neutron detection efficiencies, ε_{tn}, greater than 35% [8]. In addition,

with proper alignment, two MSND devices may be stacked to compose a single detector with potentially double the neutron detection efficiency compared to a single MSND device.

In the present work, the backfilled neutron reactive material is ^{6}LiF, which relies on the ^{6}Li(n,t)^{4}He reaction. When thermal neutrons are absorbed by ^{6}Li, a 2.73 MeV triton and a 2.05 MeV alpha particle are ejected in opposite directions. These reaction products are much more energetic than those of the ^{10}B(n,α)^{7}Li or ^{157}Gd(n,γ)^{158}Gd reactions, such that the measured signal to noise ratio is larger, thereby improving discrimination of background radiations [6]. ^{6}Li has a relatively large microscopic thermal neutron absorption cross section of 940 b. The cross section value falls rapidly with increasing neutron energy and is proportional to $1/v$ up to the neutron kinetic energy of 100 keV, where reaction resonances start to occur. In addition, the stable compound ^{6}LiF was used instead of the highly reactive lithium metal.

The present work employs previous technological methods [16], in conjunction with stacking dual-integrated detectors to achieve unmatched solid-state neutron detection efficiency. With recent advancements in inductively-coupled-plasma reactive-ion-etching (ICP-RIE) using high-aspect ratio deep etching (HARDE) techniques, along with common MEMS wet-etching techniques [6], [16]–[18], unique neutron detector microstructures have been realized. Wet-etched straight trench MSND devices have been fabricated and backfilled with nanoparticle ^{6}LiF powder neutron-absorber material. Simulated spectra for different microstructured patterns and neutron-reactive backfilled materials have been previously investigated to provide predictive information for optimal device design configurations [2], [8], [19], [20]. Note that in [8], [19], [20] the reported reaction product particle energies were inadvertently switched for the ^{10}B(n,α)^{7}Li neutron reaction. These switched energies are typographical errors and were not included in the Monte Carlo simulations. The calculated pulse-height spectra produced in [8], [19], [20] are correct.

The focus of this work involved mounting two detector chips back-to-back, along with counting electronics, and coupling them together into a single detector device. Previous work has been completed with this device [6], [7]; hereon, an effort has been made to improve the detection efficiency of the device by modifying the charge-sensing detection circuitry to account for longer charge integration time. Additionally, supplementary discussion is given in regards to a method for nano-sizing ^{6}LiF powder. For the improved dual detector device, the intrinsic detection efficiency for normal incident 0.0253 eV neutrons was found by calibrating the detector against a calibrated ^{3}He proportional counter [21]. An important clear advantage for the 3-D microstructured neutron detectors is the high efficiency
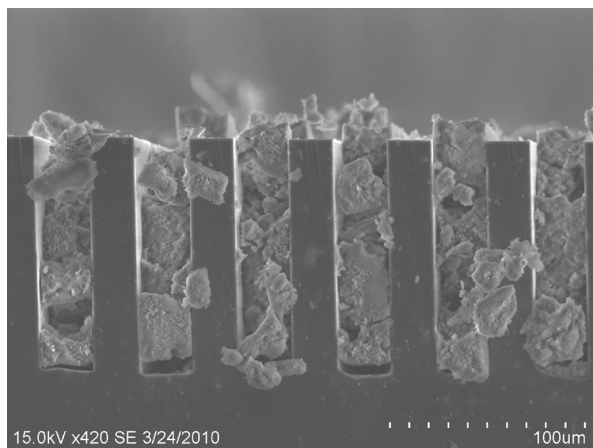
Fig. 1. A cleaved Si device with ^{6}LiF nanopowder backfilled into the wet-etched straight trench micro-structures 100 microns deep. Note that the cleaving process dislodges the tightly packed LiF material from the trenches, and is not indicative of the final backfill within the trenches.
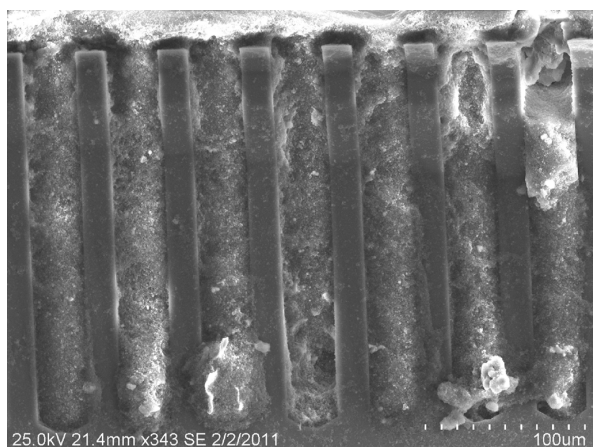

Fig. 2. ^{6}LiF nanopowder backfilled into the wet-etched straight trench micro-structures 224 microns deep.

Fig. 3. (top) Micron-sized ^{6}LiF is typical of commercially available or solution made material. Note the varying particle sizes of the cubic crystals, ranging from sub-micron to several microns. (bottom) Solution-precipitated ^{6}LiF powder backfilled into the straight trench microstructures 212 microns deep. Notice that the coarse material loosely packs into the microstructures, leaving large packing fraction voids.

achieved with a single device, which can be doubled with stacked configurations.

II. NEUTRON DETECTOR FABRICATION

A. Detector Chip Fabrication

Initially, an oxide was grown on a 10 kΩ-cm n-type Si wafer. A diffusion window was patterned and the oxide was partially removed via wet-etching. Silicon microstructures were then etched into the Si diffusion windows with a 45% KOH wet-etch submersion process at 70°C; the trench pattern, masked in the residual oxide of the diffusion window, was aligned to the $\langle 111 \rangle$ planes in a (110) orientated Si wafer. Individual detectors were batch processed on 3 inch diameter wafers, each with an active square-area of 1 cm^2. The devices reported in the present work have straight trenches etched 250 microns deep by 25 microns wide, where the trench centerlines are periodically spaced 50 microns apart. The straight trench design maintains high neutron detection efficiency while creating an opportunity to off-set stack the detector chips so as to maximize neutron absorption; for further detail see [6], [7].
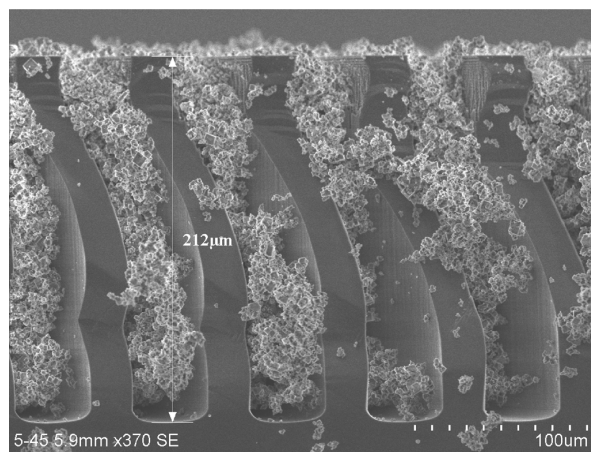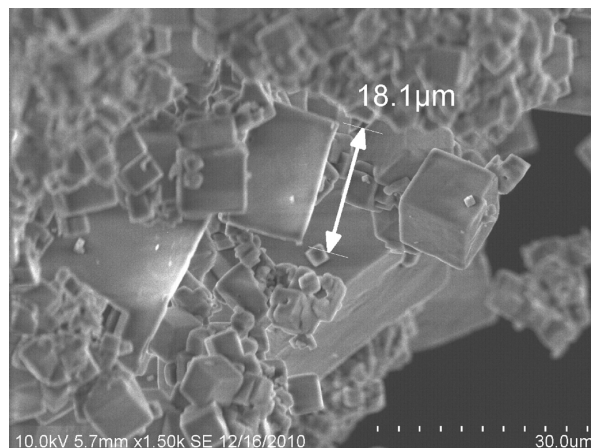
After the etch process, the wafer was chemically cleaned and p-type regions were solid-source diffused uniformly into individual device microstructures across the wafer, thereby forming pn junctions within the trenches. A Ti-Au metal contact was evaporated on the backside of the wafer to make an electrical ground contact, thereby completing the diode structure and enabling depletion through the bulk of the individual devices; for further detail of the device fabrication processes see [16].

Finally, nanoparticle ^{6}LiF powder was packed into the trenches to function as the neutron absorbing converter material (Figs. 1 and 2). The LiF material was synthesized by reacting LiOH and HF to precipitate solid LiF in 1–30 micron cubic granules (Fig. 3) [22]. The coarse LiF powder was then reduced to nanopowder through a vapor transport condensation method and mechanically pressed in the Si microstructures, such that the LiF nanopowder packs densely (Fig. 1) into the trenches with little to no void fraction; these processes are discussed in the following section.

B. Nanoparticle ^{6}LiF Powder Production

The LiF powder was produced on site by reacting ^{6}Li metal (95% enriched) from *Icon Services* with DI water to
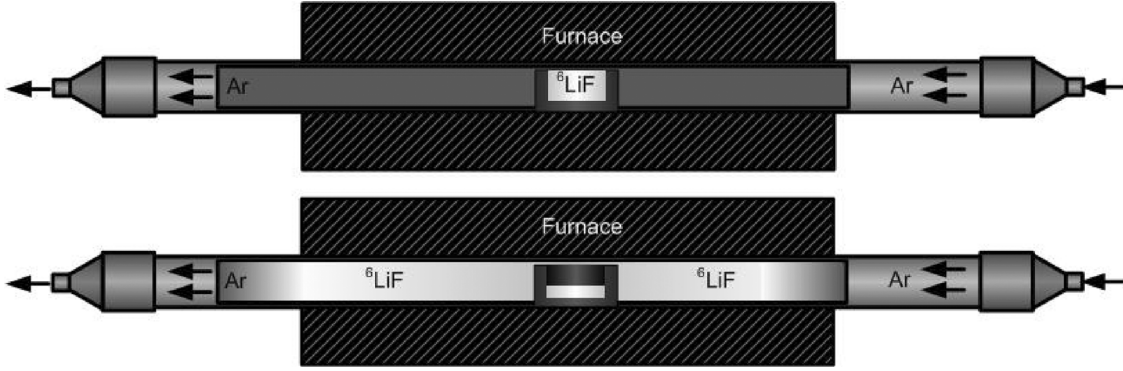
Fig. 4. (Top) LiF is loaded into a carbon crucible under an argon atmosphere and is heated to just below boiling to control volatility. (Bottom) The vapor disperses with a slight bias in the direction of the gas flow and precipitates along the surface of the furnace process tube. Remaining material can be reused in a subsequent operation.

make ^{6}LiOH and then titrating with semiconductor-grade HF, thereby precipitating ^{6}LiF. The ^{6}LiF powder that was created in this manner tends to form large, micro-sized cubic crystals as shown in Fig. 3. These large crystals tend to cause problems when backfilling the microstructured devices, such that the large sized cubic-crystals reduce the overall packing density that can be obtained within the trenches (see Fig. 3). This inefficient packing of the LiF powder within the trenches reduces the neutron absorption efficiency, and correspondingly the detection efficiency. Therefore, it has become important to reduce the crystalline size of the LiF powder in order to increase the packing density of the LiF material within the silicon devices.

Although some nanoparticle LiF material is produced during the standard precipitation process, it is not in large quantities and is mixed with the larger crystalline material. It has proven difficult and inefficient to harvest the smaller material from the batch processed material. A method for creating nanoparticle LiF powder has been developed for use in the microstructured neutron detectors. In this new method, LiF is placed in a carbon crucible inside an alumina (or SiC) furnace tube, and is heated slightly below the boiling point (refer to Fig. 4). This temperature is held for a period of time, such that the LiF volatizes inside the slightly pressurized furnace tube, produced by a flowing-gas argon atmosphere. The LiF vapor diffuses throughout the chamber, leaving the heated zone with a slight bias in the direction of the argon (Ar) gas flow and agglomerates back onto the surface of the furnace tube.

As the vapor material moves through the tube, spheres of the nano-LiF material form and agglomerate into fractals of varying orders as seen in Fig. 5. In this state, the agglomerated material, carried by the argon gas flow, is governed by aerosol dynamics of fractal agglomerates [23]. The process of collection is driven largely by thermophoresis; although, Brownian motion of the particles and electrical migration, from built-up charge on the particles themselves, may also contribute to condensation in the outer furnace zone [23]. The velocity of the nano-LiF particle, from thermophoretic forces, is described by the kinetic theory of gasses [23],

$$c_t = \frac{-3\nu\nabla T}{4(1 + \pi\alpha/8)T}, \quad (d_p \ll l_p). \qquad \text{(Eq. 1)}$$

The thermophoretic velocity c_t, varies based on the temperature of the carrier gas T, the kinematic viscosity of the gas ν, and the accommodation coefficient α, and holds true for all agglomerates whose diameter d_p is much smaller than the mean free path of the gas l_p. As the LiF vapor exits the heating zone, thermophoresis forces the agglomerated particles to the surface of the tube where they cool rapidly, and keeps larger spherical particles from forming. Van der Waals forces keep the particles on the surface of the furnace process tube. The thin layer of nanoparticle LiF, deposited throughout the tube, is then harvested. The entire process takes hours, producing a few grams of material, but can be scaled up, thereby allowing for the potential of nanoparticle LiF material mass production. Placing the material under greater scrutiny, it has been observed that the LiF material is highly electrostatic. The nanoparticle particles tend to cling together and sinter into spheres that are roughly 1 μm to 0.5 μm in diameter (see Fig. 5). The formation of the agglomerated spheres can be controlled by reducing the vaporization rate and increasing the Ar flow rate, but this change is a detriment to the production rate, which is greatly reduced.

Energy-dispersive X-ray spectral analysis (EDS) with a *Hitachi* S-3400N scanning electron microscope was conducted on the nanoparticle LiF material to probe for the presence of LiF and contaminates within the material. A representative EDS spectrum and fluorine atomic percentage of LiF particles is provided in Fig. 6. Elemental lithium X-ray response is not possible with the EDS system due to the characteristic low-energy fluorescent X-rays being absorbed in the EDS detector window. The data confirms the lack of substantial contamination of the nano-LiF material during the thermal vapor and subsequent reconstituting size-reduction processing.

The usefulness of being able to create nanoparticle LiF is not limited to MSND thermal neutron detectors. There is potential for its application in scintillators, particularly liquid scintillators, as a dispersed neutron converting material. Similar work has shown the particle size can be tuned, such that under UV illumination the photon is wavelength downshifted to a characteristically longer wavelength photon [24]. Based on this idea, a scintillation photon in a solid or liquid scintillator can be wavelength shifted to better match a photocathode for a photomultiplier tube or better couple to a solid-state diode detector. Additional conjectured advantages of using nanoparticle quantum
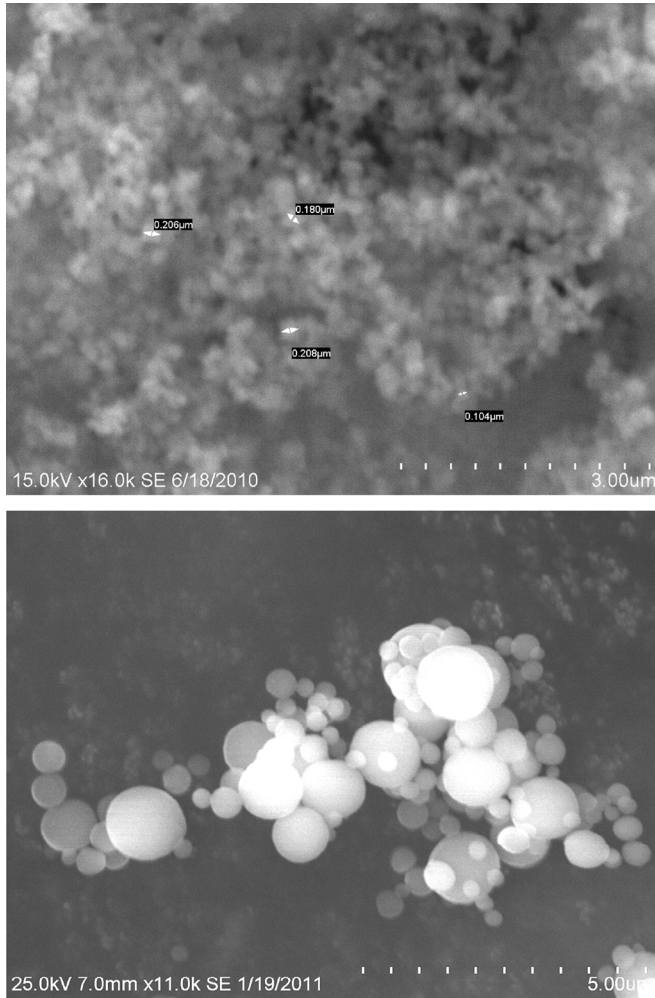
Fig. 5. (top) Nanoparticle ^{6}LiF that was produced via vaporization and (bottom) spherical sintered conglomerates of nano-material that have collected into a series of small spheres through electrostatic forces. Notice that the agglomerated spheres seem to form into emblematic fractals of varying dimension.
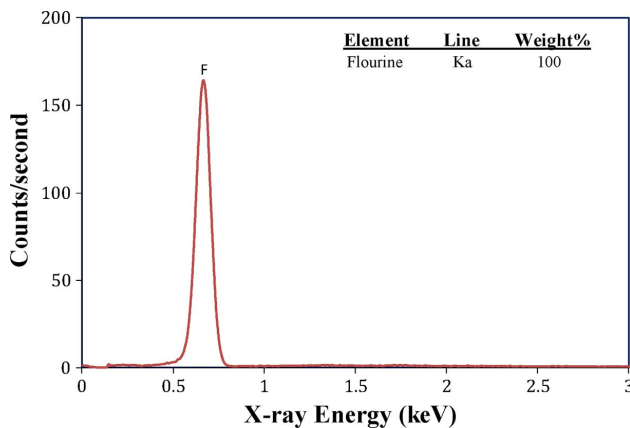

Fig. 6. EDS spectrum of the nano-LiF particles showing the dominate presence of the element fluorine when bombarded with 25 keV electrons. The energy scale was reduced from 25 keV to 3 keV because no spectral signatures were present at higher energy levels. Lithium X-ray response is not present due to X-ray absorption in the EDS detector window.

dots (QDs) as a scintillation or a wavelength shifting mechanism [25] over, or in conjunction with, fluorescent dyes is to im-

prove light collection efficiency by reducing self-absorption, to reduce nonradiative exciton recombination, and to decrease the decay-time of the induced luminescence by removing the slower multi-state luminescent dye with nanoparticle direct bandgap QD fluorescent emission [26].

C. Detector Counting Electronics

Individual device chips were then mounted as dual-integrated detector systems. The dual detector amplifying and readout electronics were specifically designed in-house and consists of a sandwiched detector board and a separate motherboard (see Fig. 7 and [7]). The separate motherboard configuration was used for research purposes as it simplifies testing multiple detector types through the use of common electronics [7]. In this configuration, the contacts of each detector are common and applied to the input of a charge sensitive preamp. In earlier work, a relatively short preamplifier charge integration time of 2 μs was used [7]; it was found in [7] that the charge drifts slowly in the weak electric potential field of the microstructure diode, a consequence of the conformal diffusion design. Charge drift simulations were completed in [7] and predicted a full charge integration time, for a 250 micron deep trench microstructured diode, of 10 μs, see Fig. 8. Therefore, the preamplifier was reconfigured for a longer charge integration time of 10 μs. Further analysis of deeper trenches was recently completed for a 350 micron deep trench microstructure where charge collection efficiency (CCE) versus collection time was simulated and is shown in Fig. 8. Notice that the CCE of the 350 micron trench device is worse than the 250 micron trench device. Hence, motivation to increase trench deep to increase neutron detection efficiency is dissuasive.

III. NEUTRON DETECTION MEASUREMENTS

Neutron counting efficiency was measured with a 0.0253 eV diffracted neutron beam from the Kansas State University TRIGA Mark II nuclear reactor [27]. The neutron flux was calibrated with a Reuter-Stokes ^{3}He gas-filled proportional detector and found to be $1.05 \pm 0.02 \times 10^3$ n cm^{-2}s^{-1}. Details of the calibration method can be found elsewhere [21]. A thorough discussion of the KSU diffracted thermal neutron beam setup, along with neutron detector calibration techniques employed by other groups, is given in [28].

A pulse-height spectrum was collected from the stacked dual-integrated microstructured detector in the diffracted neutron beam with and without a Cd shutter so as to allow the collection of responses with and without thermal neutrons. Prompt gamma-rays emitted from the thin Cd shutter appear in the spectrum as numerous pulses at low energy near the noise floor of the detector system (see Fig. 9). The neutron detection efficiency $\varepsilon_{\mathrm{MSND}}$ was calculated by dividing the summed neutron counts collected from an MSND device with an LLD set above the system noise, by the thermal neutron flux determined with a calibrated ^{3}He detector,

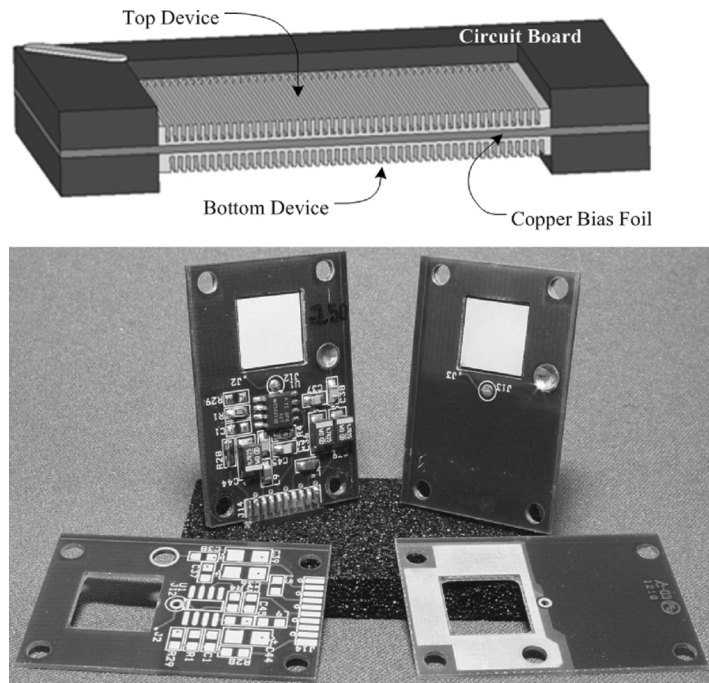$$\varepsilon_{\mathrm{MSND}} = \frac{\sum_{\mathrm{LLD}} P_n}{\Phi_n \cdot A \cdot t} \qquad \text{(Eq. 2)}$$

Fig. 7. Shown (top) is a cut-section illustration of the stacked arrangement of the dual-integrated device and (bottom) assembled 1 cm² dual-integrated packaged devices with preamplifying circuitry. The motherboard, which provides an adjustable detector bias, bias current compensation, pulse shaping and gain, an analog output for pulse-height analysis, and a "digital" output, is shown elsewhere [7].
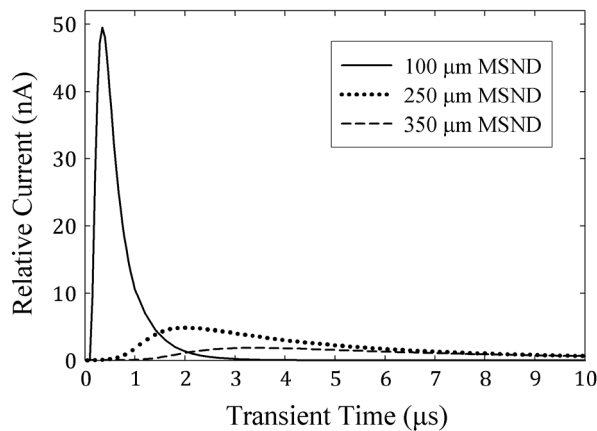

Fig. 8. *Silvaco* TCAD™ modeled transient solution of induced current versus time within 100 μm, 250 μm, and 350 μm deep straight trench MSND devices. The silicon fin and trench widths are 25 μm.

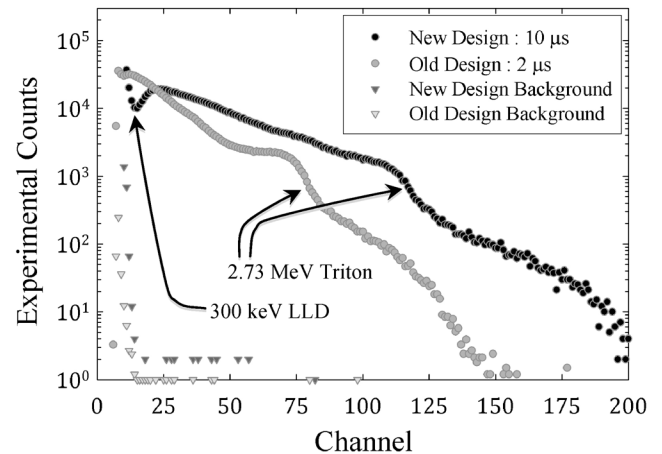Fig. 9. Pulse-height spectra comparison of the previous 2 μs charge integration-time preamp old design versus the improved 10 μs charge integration-time preamp new design for the dual-integrated 250 μm deep straight trench microstructure backfilled with ^{6}LiF. At an LLD = 15 Chn (300 keV), the measured thermal neutron detection $\varepsilon_{\mathrm{tn}}$ was 42% for the 10 μs charge integration-time preamp design.

where $\varepsilon_{\mathrm{MSND}}$ varies by the summation of P_n the MSND device pulses above some LLD, Φ_n the diffracted thermal neutron beam flux, A the MSND device active area, and t the measured count time. The neutron detection efficiency uncertainty was derived through Gaussian statistics and propagation of error. Note that if the diffracted neutron beam cross section area is smaller than the active area of the MSND device, then the device efficiency is no longer dependent on the active area A.

Shown in Fig. 9 is the measured pulse-height spectrum from the dual-integrated device, with each detector chip having 250 micron deep trenches. The single dual-integrated device works well with as little as 2 volts of applied bias. The total leakage current for the 1 cm² dual-integrated devices was 500 nA [7].

Note that in Fig. 9, the old preamp design pulse-height spectrum is shifted to lower channels than shown elsewhere for shallower trench depth designs [21], [29]. By increasing the preamp charge integration time to 10 μs for the same device, the thermal neutron irradiation pulse-height spectrum has shifted to higher channels, away from the noise/gamma-ray floor of the neutron counting system. In addition, notice the spectral shape of the 10 μs signal integration time design corresponds well with the expected results calculated elsewhere, in which a dip in the spectrum appears in the lower energy region of the pulse-height spectrum [8]. This fortuitous dip in the pulse height spectrum at

low energies allows for the trench design to be operated with an increased LLD setting over other microstructured designs [8], thereby improving gamma-ray discrimination, without severely reducing the detector efficiency.

Similar to the other tested devices with the Cd shutter closed [30], the gamma-ray component was negligible at an LLD setting above channel 11 for the 2 μs signal integration time design and channel 15 for the 10 μs signal integration time design. As previously reported, with the LLD set to channel 11 (375 keV), the intrinsic efficiency for the 2 μs signal integration time design was measured to be $37.0 \pm 0.06\%$. For the 10 μs signal integration time design, with the LLD set to channel 15 (300 keV), the intrinsic efficiency was measured to be $42.2 \pm 0.03\%$. For the 10 μs signal integration time design, with the LLD set to channel 22 (450 keV), the intrinsic efficiency was measured to be $35.8 \pm 0.04\%$.

The actual gamma-ray flux with the Cd shutter in place was not measured; however, the stacked MSND device was independently tested with a 73.1 mCi ^{137}Cs source to determine the gamma-ray detection efficiency and rejection ratio. The gamma-ray source was place 50 cm away from the detector and a pulse-height spectrum was measured. The gamma-ray detection efficiency ε_γ was determined by (3),

$$\varepsilon_\gamma = \frac{\sum_{\mathrm{LLD}} P_\gamma}{\Phi_\gamma \cdot A \cdot t}, \qquad \text{(Eq. 3)}$$

where ε_γ varies by the summation of P_γ the MSND device pulses above some LLD, Φ_γ the gamma-ray source flux through the detector which was $8.60 \times 10^4 \ \gamma \ \mathrm{cm}^{-2}\mathrm{s}^{-1}$, A the MSND device active area, and t the measured count time. The neutron to gamma-ray rejection ratio n/γ was determined by (4),

$$\frac{n}{\gamma} = \frac{\varepsilon_{\mathrm{MSND}}}{\varepsilon_\gamma}, \qquad \text{(Eq. 4)}$$

where n/γ rejection ratio varies by $\varepsilon_{\mathrm{MSND}}$ the MSND device neutron detection efficiency and ε_γ the MSND device gamma-ray detection efficiency.

The gamma-ray pulse-height spectrum response is shown in Fig. 10. Notice that a majority of the dual-integrated detector's response to the ^{137}Cs source is in low-energy channels, but is above the background count response, which may be due to pulse pileup from the relatively high gamma-ray flux impinging on the MSND device. In addition, the stacked MSND gamma-ray response measurement was performed in the KSU reactor bay; hence, some higher energy measured events may be to background neutron radiation.

As shown in Fig. 11, with the LLD set at 300 keV, the gamma-ray detection efficiency was determined to be less than 1.87×10^{-5} measured-event per gamma ray, with a n/γ rejection ratio of 2.20×10^4 neutrons per gamma ray, and with the LLD set to 450 keV the gamma-ray detection efficiency is less than 3.49×10^{-7} measured-event per gamma ray, with a n/γ rejection ratio of 1.00×10^6 neutrons per gamma ray. Also notice in Fig. 11, that the n/γ rejection ratio is almost constant past LLD channel 35, which is because only a few counts were recorded above this channel. In addition, because the n/γ rejection ratio follows as inverse proportional to the gamma-ray
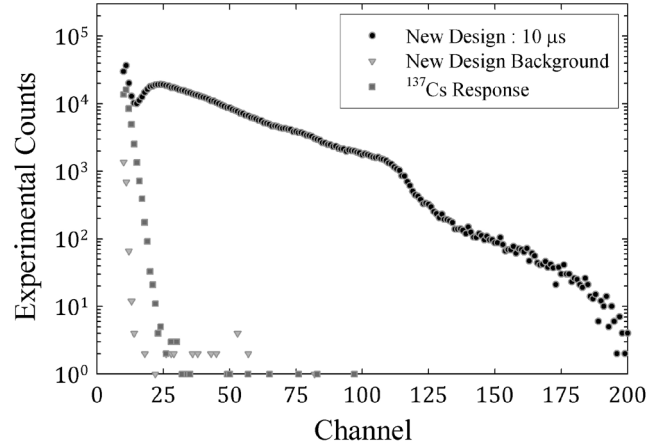

Fig. 10. Measured ^{137}Cs gamma-ray irradiation and neutron irradiation pulse-height spectral features for the stacked dual-integrated 250 micron deep straight trench MSND device with the 10 μs signal integration time design.

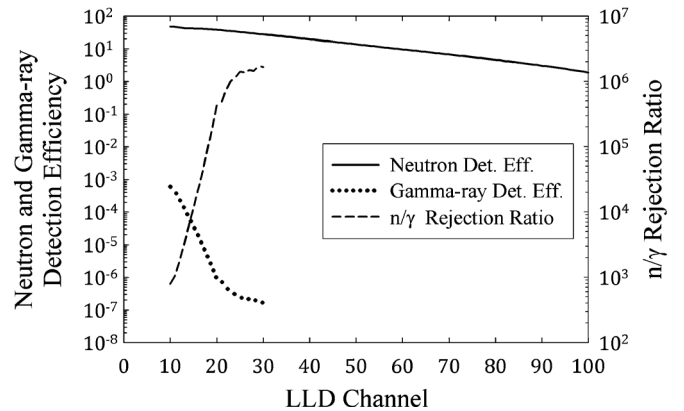

Fig. 11. Comparison of the measured neutron detection efficiency, the measured ^{137}Cs gamma-ray detection efficiency, and the n/γ rejection ratio of the dual-integrated stacked 1 cm^2 MSND device.

detection efficiency, which goes to zero at channel 98, the n/γ rejection ratio becomes infinite. The deeper micro-structured trenches and dual-integrated devices show a slight reduction in pulse height, which can decrease the gamma-ray rejection ratio. Yet, in the present work, this pulse height shift does not appear to be severe, and has sufficiently moved away from the noise floor with the increased preamp charge integration time. Note that the gamma-ray interactions within the device also diminish with deeper microstructures, due to less interaction volume, thereby allowing for smaller LLD settings resulting in superior gamma-ray discrimination.

IV. CONCLUSION

A dual-integrated, 1 cm^2 straight trench microstructured Si detector, backfilled with ^{6}LiF powder has been characterized for neutron sensitivity in a diffracted 0.0253 eV thermal neutron beam from a TRIGA Mark II nuclear reactor. An important clear advantage for the dual-integrated micro-structured neutron detector design is the high efficiency achieved by appropriately stacking two detector chips into a single device. Efficiency is dramatically increased by capturing streaming neutrons from the first detector. The dual-integrated detector with two 250 micron deep trenched devices achieved 42% intrinsic efficiency,
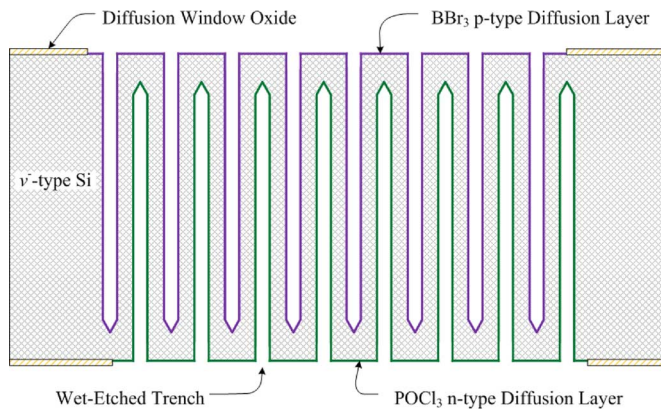
Fig. 12. Illustration of advanced microstructure design with interlaced microstructures that are etched from both sides of the Si diode to improve charge drifting electric field potential.

which is a total increase of 5% detection efficiency over the previous preamplifying circuitry design. Finally, the gamma-ray rejection for the dual-integrated stacked device was high, with prompt Cd and ^{137}Cs gamma rays in the low energy to noise end of the pulse height spectrum, which is due to many combined effects explained elsewhere [8].

To improve charge capture efficiency and shorten the signal integration time, future work should be dedicated to fabrication of interlaced microstructures that are etched from both sides of the Si diode, as shown in Fig. 12, which was first described elsewhere [31]. Though more difficult to fabricate, the electric field will be uniformly distributed across the Si detector volume and the signal integration time necessary to collect all of the produced charge will be reduced and not limited by increased microstructure depth.

REFERENCES

[1] D. S. McGregor *et al.*, "New surface morphology for low stress thin-film-coated thermal neutron detectors," *IEEE Trans. Nucl. Sci.*, vol. 49, no. 4, pp. 1999–2004, Aug. 2002.

[2] J. K. Shultis and D. S. McGregor, "Efficiencies of coated and perforated semiconductor neutron detectors," *IEEE Trans. Nucl. Sci.*, vol. 53, no. 3, pp. 1659–1665, Jun. 2006.

[3] W. J. McNeil *et al.*, "Perforated diode fabrication for neutron detection," in *IEEE Nucl. Sci. Sym. Conf. Rec.*, 2006, pp. 3732–3735.

[4] Q. Jahan, E. Patterson, B. Rice, W. L. Dunn, and D. S. McGregor, "Neutron dosimeters employing high-efficiency perforated semiconductor detectors," *Nucl. Instrum. Meth.*, vol. B263, pp. 183–185, 2007.

[5] C. J. Solomon, J. K. Shultis, W. J. McNeil, B. B. Rice, and D. S. McGregor, "A hybrid method for coupled neutron-ion transport calculations for ^{10}B and ^{6}LiF coated and perforated detector efficiencies," *Nucl. Instrum. Meth.*, vol. A580, pp. 326–330, 2007.

[6] S. L. Bellinger *et al.*, "Characteristics of the stacked microstructured solid-state neutron detector," in *Proc. SPIE—Int. Soc. Opt. Eng.*, 2010, pp. 78050-16.

[7] S. L. Bellinger *et al.*, "Enhanced variant designs and characteristics of the microstructured solid-state neutron detector," *Nucl. Instrum. Meth.*, vol. A652, pp. 387–391, 2011.

[8] J. K. Shultis and D. S. McGregor, "Design and performance considerations for perforated semiconductor thermal-neutron detectors," *Nucl. Instrum. Meth.*, vol. A606, pp. 608–636, 2009.

[9] D. S. McGregor *et al.*, "Design considerations for thin film coated semiconductor thermal neutron detectors, Part I: Basics regarding alpha particle emitting neutron reactive films," *Nucl. Instrum. Meth.*, vol. A500, pp. 272–308, 2003.

[10] R. A. Muminov and L. D. Tsvang, "High-efficiency semiconductor thermal-neutron detectors," *Soviet Atomic Energy*, vol. 62, no. 4, pp. 316–319, 1987.

[11] J. Schelten, M. Balzhauser, F. Hongesberg, R. Engels, and R. Reinartz, "A new neutron detector development based on silicon semiconductor and ^{6}LiF converter," *Physica B*, vol. 234–236, pp. 1084–1086, 1997.

[12] C. P. Allier, *Micromachined Si-Well Scintillator Pixel Detectors*. The Netherlands: DUP Science, 2001.

[13] J. Uher *et al.*, "Characterization of 3-D thermal neutron semiconductor detectors," *Nucl. Instrum. Meth.*, vol. A576, pp. 32–37, 2007.

[14] R. J. Nikolic *et al.*, "Nine element Si-based pillar structured thermal neutron detector," in *Proc. SPIE—Int. Soc. Opt. Eng.*, 2010, p. 78050.

[15] J. Dingley, Y. Danon, N. LiCausi, J. Q. Lu, and I. B. Bhat, "Optimization of a novel solid-state self powered neutron detector," in *Proc. Int. Conf. Math., Comp. Meth. Reactor Phys.*, LaGrange Park, 2009.

[16] S. L. Bellinger, W. J. McNeil, and D. S. McGregor, "Improved fabrication technique for microstructured solid-state neutron detectors," in *Proc. MRS Spring Meeting*, 2009, pp. 57–65.

[17] S. L. Bellinger *et al.*, "Characteristics of 3-D micro-structured semiconductor high efficiency neutron detectors," *IEEE Trans. Nucl. Sci.*, vol. 56, no. 3, pp. 742–746, 2009.

[18] K. E. Bean and R. J. Lawson, "Application of silicon crystal orientation and anisotropic effects to the control of charge spreading in devices," *IEEE J. Solid-State Circuits*, vol. SC-9, no. 3, pp. 111–117, 1974.

[19] J. K. Shultis and D. S. McGregor, "Calculation of Ion Energy-Deposition Spectra in Silicon, Lithium-Fluoride, Boron, and Boron Carbide," 2004, Engineering Experiment Station 299, Manhattan, KS.

[20] D. S. McGregor *et al.*, "Perforated diode neutron detector modules fabricated from high-purity-silicon," *Radiation Phys. Chem.*, no. 78, pp. 195–207, 2009.

[21] D. S. McGregor, W. J. McNeil, S. L. Bellinger, T. C. Unruh, and J. K. Shultis, "Microstructured semiconductor neutron detectors," *Nucl. Instrum. Meth.*, vol. A608, pp. 125–131, 2009.

[22] D. S. McGregor *et al.*, "Perforated semiconductor neutron detector modules," in *Proc. 32nd Ann. GOMACTech Conf.*, 2007.

[23] S. Friedlander, *Smoke, Dust, and Haze: Fundamentals of Aerosol Dynamics*, 2nd ed. New York: Oxford, 2000.

[24] D. H. A. Ponce, S. Cingarapu, and K. J. Klabunde, "Nanoparticles prepared by salt vapor-solvent vapor condensation and controlled nucleation: Metal sulfides (ZnS, CdS, CdSe, PbS), and metal halide (LiF). Size, aggregates, structures, digestive ripening, superlattices, and impregnations," *Adv. Functional Mater.*, no. 17, pp. 3562–3568, 2007.

[25] S. Cingarapu, "Synthesis of CdSe quantum dots by evaporation of bulk CdSe using SMAD and digestive ripening processes," *Chem. Mater.*, vol. 21, no. 7, pp. 1248–1252, 2009.

[26] S. Stobbe, "Frequency dependence of the radiative decay rate of excitons in self-assembled quantum dots: Experiment and theory," *Phys. Rev. B, Condens. Matter Mater. Phys.*, vol. 80, no. 15, p. 155307, 2009.

[27] T. C. Unruh, "Development of a Neutron Diffraction System and Neutron Imaging System for Beamport Characterization," Ph.D. dissertation, Kansas State Univ., Manhattan, 2009.

[28] D. S. McGregor and J. K. Shultis, "Reporting detection efficiency for semiconductor neutron detectors; a need for a standard," *Nuc. Instrum. Meth.*, vol. A632, pp. 167–174, 2011.

[29] D. S. McGregor, S. L. Bellinger, W. J. McNeil, and T. C. Unruh, "Micro-structured high-efficiency semi-conductor neutron detectors," in *Proc. IEEE Nucl. Sci. Sym. Conf. Rec.*, 2008, pp. 446–448.

[30] S. L. Bellinger, W. J. McNeil, and D. S. McGregor, "Variant designs and characteristics of improved microstructured solid-state neutron detectors," in *Proc. IEEE Nucl. Sci. Sym. Conf. Rec.*, 2009, pp. 986–989.

[31] D. S. McGregor and R. T. Klann, "High-Efficiency Neutron Detectors and Methods of Making the Same," U.S. Patent 7 164 138, Jan. 16, 2007.